

Review of structure-dependent transport properties in $SrIrO_3$

Mingjia Chen(陈铭嘉), Shuanhu Wang(王拴虎), Yirui Chen(陈一瑞), Dailei Ren(任玳蕾), Jiatai Wang(王加泰), Jialiang Yao(姚佳良), Kexin Jin(金克新), and Hong Yan(闫虹)

Citation: Chin. Phys. B, 2026, 35 (**6**): 067301. DOI: 10.1088/1674-1056/ae4b28
http://cpb.iphy.ac.cn; http://iopscience.iop.org/cpb

What follows is a list of articles you may be interested in

Type-II Dirac nodal chain semimetal CrB_4

Xiao-Yao Hou(侯逍遥), Ze-Feng Gao(高泽峰), Peng-Jie Guo(郭朋杰), Jian-Feng Zhang(张建丰), and Zhong-Yi Lu(卢仲毅)

Chin. Phys. B, 2026, 35 (**1**): 017301. DOI: 10.1088/1674-1056/ae172b

Intrinsic higher-order topological states in two-dimensional honeycomb quantum spin Hall insulators

Sibin Lü(吕思彬) and Jun Hu(胡军)

Chin. Phys. B, 2025, 34 (**11**): 117303. DOI: 10.1088/1674-1056/addcd2

Observation of distinct Kondo effect and anomalous Hall effect in V self-intercalated layered antiferromagnet V_5S_8 crystals

Yaofeng Xie(谢耀锋), Senhao Lv(吕森浩), Qi Qi(齐琦), Guojing Hu(胡国静), Ke Zhu(祝轲), Zhen Zhao(赵振), Guoyu Xian(冼国裕), Yechao Han(韩烨超), Ruwen Wang(王汝文), Chenyu Bai(白晨宇), Lihong Bao(鲍丽宏), Xiao Lin(林晓), Hui Guo(郭辉), Haitao Yang(杨海涛), and Hong-Jun Gao(高鸿钧)

Chin. Phys. B, 2025, 34 (**8**): 087303. DOI: 10.1088/1674-1056/add5cd

Magnetotransport properties of two-dimensional tellurium at high pressure

Huiyuan Guo(郭慧圆), Jialiang Jiang(姜家梁), Boyu Zou(邹博宇), Jie Cui(崔杰), Qinglin Wang(王庆林), Haiwa Zhang(张海娃), Guangyu Wang(王光宇), Guozhao Zhang(张国召), Kai Wang(王凯), Yinwei Li(李印威), and Cailong Liu(刘才龙)

Chin. Phys. B, 2025, 34 (**8**): 087301. DOI: 10.1088/1674-1056/add5c9

Correlated physics, charge and magnetic orders in moiré kagomé systems

Zhaochen Liu(刘兆晨) and Jing Wang(王靖)

Chin. Phys. B, 2025, 34 (**2**): 027304. DOI: 10.1088/1674-1056/ad9ffa

---

REVIEW

Review of structure-dependent transport properties in $SrIrO_3$

Mingjia Chen(陈铭嘉), Shuanhu Wang(王拴虎), Yirui Chen(陈一瑞), Dailei Ren(任玳蕾), Jiatai Wang(王加泰), Jialiang Yao(姚佳良), Kexin Jin(金克新), and Hong Yan(闫虹)†

Shaanxi Key Laboratory of Condensed Matter Structures and Properties & MOE Key Laboratory of Materials Physics and Chemistry under Extraordinary Conditions, School of Physical Science and Technology, Northwestern Polytechnical University, Xi'an 710072, China

(Received 6 January 2026; revised manuscript received 12 February 2026; accepted manuscript online 27 February 2026)

As a prominent member of the 5d transition metal oxide family, $SrIrO_3$ has emerged as a critical platform for investigating correlated topological states due to the complex interaction between strong spin–orbit coupling, moderate electron correlations, and structural flexibility. This review summarizes recent advances in the study of transport properties of $SrIrO_3$. Both bulk and thin-film forms of this material exhibit a range of transport phenomena, including metallic conductivity modulated by correlation effects, large anomalous Hall effects originating from non-trivial band topology, and metal–insulator transitions induced by external strain, electric fields, or reduced dimensionality. In heterostructures and superlattices, in particular, interfacial charge transfer, orbital reconstruction, and proximity effects can give rise to emergent magnetism and topological transport, such as highly efficient spin–orbit torques. These observed behaviors suggest the potential realization of a Weyl semimetal or topological crystalline insulator phase in $SrIrO_3$. Recent progress in $SrIrO_3$ underscores the importance of further exploring novel quantum phases within its phase diagram via multi-field control, clarifying the underlying microscopic mechanisms using advanced characterization techniques, and developing low-power electronics and spintronic devices leveraging its intertwined topological and correlated properties.

Keywords: 5d iridates, $SrIrO_3$ films, spin–orbit coupling, proximity-induced magnetism

PACS: 73.40.–c, 73.61.–r, 72.25.–b, 75.76.+j

DOI: 10.1088/1674-1056/ae4b28 **CSTR:** 32038.14.CPB.ae4b28

1. Introduction

Research has shown that transition metal oxide films exhibit abundant exotic physical properties.[1–4] In recent years, the spin–orbit coupling (SOC) effect has again attracted extensive research interest, encompassing phenomena such as exchange interactions,[5–7] magnetoelectricity,[8,9] the spin Hall effect (SHE)[10,11] and Fermi surface topology.[12] The Ruddlesden–Popper series $Sr_{n+1}Ir_nO_{3n+1}$ constitutes a prototypical class of 5d transition metal oxides. Among them, the perovskite $SrIrO_3$ ($n = \infty$, hereafter abbreviated as SIO) is a strongly correlated paramagnetic metal that exhibits non-Fermi-liquid behavior.[13–16] In such oxides, rich quantum phenomena emerge from the complex interplay between charge, spin and orbital degrees of freedom, driven by substantial electron correlations. Iridium-based 5d systems, in particular, occupy a central position in condensed matter research due to the coupled spin–orbital/charge–lattice interactions arising from strong SOC, moderate electron correlation (U) and the spatially extended character of 5d orbitals.[17–20] The broader radial distribution of 5d electrons (e.g., in Ir^{5+}) promotes enhanced hybridization, situating these materials in a critical regime where the Coulomb repulsion energy is comparable with the bandwidth (W). This delicate equilibrium makes their electronic ground states highly sensitive to external perturbations — such as epitaxial strain, interfacial engineering and electrostatic gating — establishing SIO as a versatile platform for exploring the interplay between strong correlations and topological physics. As a prototypical 5d transition metal oxide, SIO resides in a regime where U and strong SOC, stemming from the high atomic number of Ir, are of comparable magnitude. This intricate interplay, further modulated by perovskite-related structural distortions and epitaxial strain, dictates the material's band topology and electronic phase transitions. Consequently, these attributes establish SIO as an ideal playground for exploring the complex competition between relativistic effects, electronic correlations and crystal field environments.

The unique electronic structure of SIO originates from the delicate interplay between crystal field splitting, strong SOC ($\sim$ 0.4–0.5 eV), and $U \approx$ 1–2 eV within the IrO_6 octahedral framework.[21,22] In this configuration, strong SOC splits the t_{2g} band into a higher-lying $J_{\rm eff} = 1/2$ doublet and a lower-lying $J_{\rm eff} = 3/2$ quartet. When electron correlations act on the $J_{\rm eff} = 1/2$ band, a Mott-type gap can open, driving the system toward an insulating state.[23] The comparable energy scales of Hund coupling in crystal fields, SOC, and SIO result in significant mixing between $J_{\rm eff} = 1/2$ and $J_{\rm eff} = 3/2$ states, indicating that SIO is located in the Mott–Slater region and exhibits a rich variety of quantum phenomena.[24–26]

In addition, SIO has been identified as a symmetry-

†Corresponding author. E-mail: yanh@nwpu.edu.cn

© 2026 Chinese Physical Society and IOP Publishing Ltd. All rights, including for text and data mining, AI training, and similar technologies, are reserved.

protected Dirac semimetal, where the Dirac state is stabilized by the combination of time-reversal symmetry and nonsymmorphic space group symmetry.[18,27–29] The $J_{\rm eff} = 1/2$ band crosses the Fermi level, forming a Dirac-cone-type nontrivial band crossing. This band structure is the root cause of the intrinsic SHE and topological surface states.[30,31] First-principles calculations by Takayama *et al.* have confirmed the formation and topological protection of these Dirac points,[32] which persist in the presence of strong SOC and structural asymmetry.[28] Moreover, SIO has characteristics that are located at the Mott insulating phase boundary, and it also exhibits strong electronic correlation effects.[33] It has also been theoretically linked to other topological states, including Weyl semimetallic properties,[34] critical quantum states,[35] and topological non-trivial states.[36] These intriguing properties establish SIO as a new paradigm material for spintronics research.[37–41]

SIO exists in various crystal structures and polymorphs, with the orthorhombic perovskite structure SIO being the most extensively studied. Zhao *et al.* successfully achieved the epitaxial growth of high-quality monoclinic SIO films on $SrTiO_3$ (STO) substrates with perovskite SIO buffer layers.[42] Synthesizing the perovskite-phase SIO in bulk form has historically posed considerable challenges. Early work by Longo *et al.* determined that under ambient pressure the thermodynamically stable phase of bulk SIO adopts a monoclinic crystal structure (space group $C2/c$) rather than the perovskite structure.[43] Achieving the orthorhombic perovskite phase (*Pbnm*) requires high-temperature and high-pressure conditions (typically > 1000 °C and > 4 GPa).[44,45] Consequently, epitaxial stabilization in thin-film form has become the primary trajectory for investigating perovskite SIO. Various deposition techniques, including pulsed laser deposition (PLD), molecular beam epitaxy, sputtering, and metal–organic chemical vapor deposition, have been utilized to fabricate SIO thin films and superlattices.[46] Among these methods, PLD is the most widely used technique for fabricating high-quality heterostructures. Using PLD, thin films can be grown in a two-dimensional, layer-by-layer mode on perovskite substrates such as STO, enabling precise thickness control down to the single-unit-cell level and facilitating the exploration of dimensional confinement effects.[47]

Research has shown that the ground state of SIO can be highly tunable by applying external stimuli such as epitaxial strain,[48] chemical doping,[49] and external electric fields,[50,51] as well as artificial structural design.[52] These approaches offer a promising pathway toward engineering unconventional functional properties.[53] In this review, we systematically summarize recent key observations on the growth, physical properties, and quantum engineering of SIO-based heterostructures. By organizing the discussion according to structural dimensionality — from single-layer and bilayer films to multilayer and superlattice architectures — we aim to establish a coherent framework for understanding how electronic behavior is transformed. This dimensional perspective provides valuable insights for exploiting emergent functionalities in strongly SOC 5d oxide systems.

2. Electronic and transport properties of $SrIrO_3$

2.1. Electronic and transport properties of $SrIrO_3$ single-layer films

2.1.1. Substrate-induced strain and lattice mismatch

Discrepancies in the lattice constants between the thin-film material and the substrate (Fig. 1(a)) induce epitaxial strain to satisfy interfacial matching requirements during growth. Consequently, substrate engineering serves as a pivotal mechanism for tuning the lattice mismatch, thereby modulating the internal stress of the film. The fundamental mechanisms of stress regulation and the resulting transport properties are elucidated in Subsection 2.1.3. As the lattice mismatch intensifies, the system undergoes a metal–insulator transition (MIT).[54] In the presence of strong SOC, an increase in the degree of structural disorder triggers non-Fermi liquid behavior, driven by localization effects and enhanced electron–electron correlations.[16] Further escalation of disorder may lead the system into a non-canonical Mott–Anderson–Griffiths transition, resulting in a strain-dependent MIT,[45,55,56] as revealed in Fig. 1(b).

The $J_{\rm eff} = 1/2$ band of $SrIrO_3$ is a semimetallic band with an equal number of electrons and holes, making its electronic properties highly susceptible to strain modulation. According to the lattice constants of different substrates, lattice mismatch strain can be divided into compressive strain and tensile strain. The band structure of $SrIrO_3$ is particularly sensitive to compressive strain, which enhances U in $SrIrO_3$ thin films, thereby reducing W and changing the disorder parameter (U/W).[45] Under sufficiently high compressive strain, the system transitions into a fully insulating state. Compressive strain also enhances the asymmetry of electron and hole carrier mobility in $SrIrO_3$ thin films, resulting in a transition from nonlinear to linear Hall behavior accompanied by a decrease in carrier concentration.[23] By choosing substrates to generate different lattice strains, Zhang *et al.* observed such nonlinear-to-linear variations in the Hall effect of $SrIrO_3$ thin films.[57] The electronic band structure of compressively strained $SrIrO_3$ films, calculated using a tight-binding Hamiltonian, is presented in Fig. 1(c). For $SrIrO_3$ thin films on $(La,Sr)(Al,Ta)O_3$ substrates, compressive strain shifts the hole branch of the Fermi level downward, giving rise to a nonlinear Hall effect. In contrast, tensile strain exerts only a minor influence on the asymmetry of electron–hole mobility.

Furthermore, the choice of substrate allows for the design of distinct spin textures in momentum space. The nonlinear planar Hall effect (NPHE) can be induced in various materials with strong spin–orbit interaction through epitaxial strain. Kozuka *et al.* compared the NPHE signals in SIO thin films grown on different substrates.[58] As shown in Fig. 1(d), the amplitude of the second-harmonic signal varies markedly with substrate choice. The strength, sign, and anisotropy of the signal are modulated by the in-plane symmetry of the substrate. These nonlinear responses originate from complex spin textures within two Dirac bands, driven by antisymmetric spin–orbit interactions, and sensitively reflect the spin-texture anisotropy of the Dirac bands.

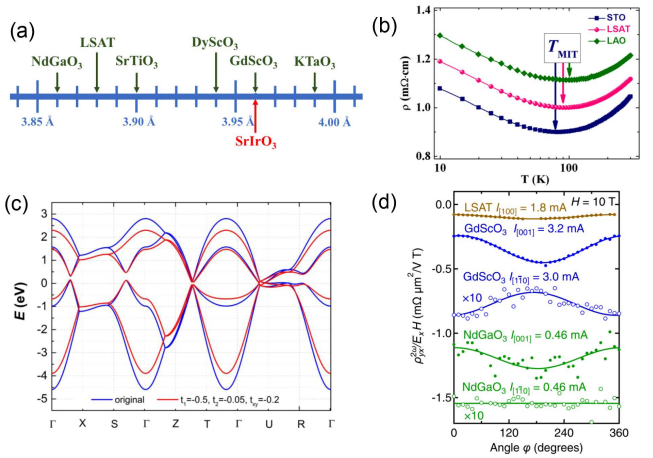


Fig. 1. (a) Cubic and/or pseudocubic lattice constants of SIO and various substrates. (b) Temperature dependence of the resistivity of SIO thin films grown on different substrates, showing the MIT. Reproduced with permission from Ref. [55] from AIP Publishing, Copyright 2015. (c) Electronic band structure of SIO films under different compressive strains. Reproduced with permission from Ref. [57] from American Physical Society, Copyright 2015. (d) Second harmonic planar Hall resistance of SIO films grown on various substrates. Reproduced with permission from Ref. [58].

2.1.2. Thickness-dependent properties

Through precise control of the critical film thickness, the electronic structure, lattice strain, and quantum confinement effects can be effectively modulated. In thin-film physics, reducing the film thickness leads to a reduced coordination number. This decrease subsequently influences band filling and narrows W,[59] while concurrently enhancing U/W.[60] Beyond intrinsic electronic shifts, reducing the thickness typically decreases the grain size and increases the density of grain boundaries.[61] This proliferation of structural defects amplifies the effective disorder, ultimately precipitating a thickness-induced MIT.[62] Additionally, reducing the film thickness enhances lattice strain, increases defects, and induces complex interactions between the substrate and the film, giving rise to novel physical phenomena.[56,63,64] Modulating the film thickness not only alters its intrinsic properties but also enables the emergence of new quantum phenomena and functional characteristics.[65,66]

In SIO thin films, the MIT is primarily driven by disorder, manifesting as an Anderson-type transition. In the vicinity of this transition, significant negative magnetoresistance (MR) is observed, a hallmark of weak localization (WL) effects in the semimetallic regime (Figs. 2(a) and 2(b)).[45,56] The charge transport mechanism evolves significantly with decreasing thickness. In thicker films, the resistivity is dominated by electron–electron and electron–boson scattering. However, as the thickness decreases and the system approaches a localized state, WL effects begin to manifest. Through the fitting analysis of temperature-dependent resistance as illustrated in Fig. 2(c), it can be found that the conductive carriers in SIO mainly scatter via electron–boson interactions.[67] As the film approaches the insulating limit, the transport behavior shifts toward the variable range hopping (VRH) model. For ultra-thin films, the conductivity often conforms to the two-dimensional Mott VRH equation, signifying that Anderson localization is the primary conduction mechanism (Fig. 2(d)).[68] Zhang *et al.* observed a crossover from two-dimensional Mott VRH to Efros–Shklovskii VRH at low temperatures (10 K) as thickness is further reduced.[69] This transition highlights the burgeoning role of U in the strongly localized regime.

The synergy between Mott-type correlation and Anderson-type disorder leads to a localized state characterized by an increased effective mass and suppressed kinetic energy, further bolstering the U/W ratio. Owing to the suboptimal sample quality in previous studies, the MIT induced by stress and other factors may be extrinsic. Remarkably, Groenendijk *et al.* systematically reduced the thickness of SIO films and observed that the MIT occurs between 4 unit cells (u.c.) and 3 u.c., with the system transitioning from a semimetallic state to an antiferromagnetic (AFM) insulating state.[70] This transformation into an intrinsic, thickness-driven quantum phenomenon marks the evolution of SIO from a three-dimensional semimetallic state to a two-dimensional confined system. It is closely linked to the theoretical prediction of topological state transitions. That study, by achieving atomically flat interfaces and precise control over the unit cell structure, is the first to eliminate non-intrinsic scattering and explore the intrinsic quantum transport behavior. As shown in Fig. 2(e), the calculated results further suggest that the emergence of long-range magnetic order is accompanied by the opening of an energy gap.[70] Consistent with the behavior of perovskite SIO, the study by Zhao *et al.* demonstrates that monoclinic SIO thin films undergo an MIT as the thickness is reduced. Upon reaching a critical thickness, a thickness-driven magnetic phase transition occurs, with the system evolving from a paramagnetic semimetal into a magnetic insulator.[42]

Film thickness can be controlled by adjusting the growth time and growth rate. Additionally, growth kinetics (e.g., growth rate) play a crucial role in tuning the carrier density. Yang *et al.* demonstrated that suppressing the carrier density can quench WL-induced negative MR, instead promoting weak antilocalization — a phenomenon fundamentally driven by the strong SOC inherent in the Ir 5d orbitals.[71]

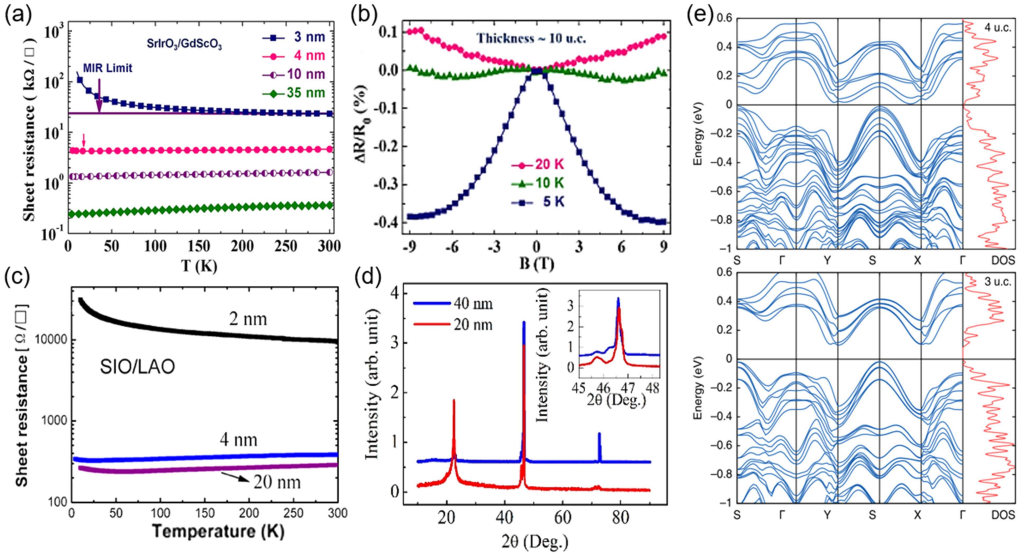


Fig. 2. (a) Temperature dependence of the resistance of SIO thin films with different thicknesses grown on $GdScO_3$ substrates. Reproduced with permission from Ref. [45] from AIP Publishing, Copyright 2014. (b) Temperature-induced sign transition of MR in SIO thin films. Reproduced with permission from Ref. [56] from Elsevier, Copyright 2017. (c) Temperature dependence of the sheet resistance of SIO thin films with varying thicknesses grown on $LaAlO_3$ substrates. Reproduced with permission from Ref. [67]. (d) X-ray scan results of SIO thin films with varying thicknesses on STO substrates. Reproduced with permission from Ref. [68] from AIP Publishing, Copyright 2019. (e) Energy dependence of the density of states for SIO films of different thicknesses on STO substrates. Reproduced with permission from Ref. [70] from American Physical Society, Copyright 2017.

2.1.3. External modulation of transport properties

Multiple approaches have been developed to modulate the transport characteristics of SIO thin films, among which electric fields constitute one of the most versatile and widely used control parameters. Electric fields can regulate transport behavior either through conventional electrostatic tuning or by modifying polarization states. More importantly, they can drive the migration of oxygen ions (or oxygen vacancies) in oxide lattices, offering an effective route to inducing topological phase transitions via oxygen incorporation or depletion.[72] $PbMg_{1/3}Nb_{2/3}O_3$-$PbTiO_3$ (PMN–PT) is a well-established piezoelectric material capable of generating large, reversible strain under applied electric fields. Owing to lattice matching and epitaxial coherence, efficient strain transfer can be achieved across the SIO/PMN–PT interface. Li *et al.* demonstrated that applying an electric field along the thickness direction of the PMN–PT substrate in SIO/PMN–PT heterostructures enables continuous tuning of the electronic transport properties of SIO. This modulation originates from a combination of non-180° ferroelectric domain rotation, intrinsic piezoelectric deformation and the rhombohedral to tetragonal phase transition in the PMN–PT layer. Concurrently, the MR of the SIO thin film exhibits pronounced electric field dependence, as illustrated in Fig. 3(a), highlighting electric field-controlled lattice strain as a powerful and straightforward means for probing strain–transport coupling in 5d iridate thin films.[73]

In condensed matter physics, strain serves as a fundamental lever for engineering the crystal field environment. By altering lattice constants, strain can lift the degeneracy of energy levels, reconstruct orbital configurations and tune the strength of SOC and electron–phonon coupling. These microscopic modifications culminate in macroscopic phenomena, such as the MIT and paraelectric to ferroelectric transitions.[44] As discussed previously, biaxial strain — imposed by selecting substrates with varying lattice constants — can profoundly reshape the physical properties of SIO.[72] Specifically, compressive strain has been shown to enhance resistivity and precipitate a MIT.[56,74] Therefore, stress is a very effective means of regulating the physical properties of oxide thin films.

First-principles calculations by Yuan *et al.* on tetragonal SIO under epitaxial strain qualitatively elucidate magnetic transitions using the Stoner model. Their lattice dynamics simulations revealed phonon instabilities under both compressive and tensile regimes (Figs. 3(b) and 3(c)), pointing toward a potential polar metallic state — a rare phase where inversion symmetry is broken in a conducting medium.[75] Beyond uniform strain, Gu *et al.* identified a stress gradient at the SIO/$NdGaO_3$ interface. This gradient induces a continuous evolution of the lattice constant across successive layers (Fig. 3(d)), which breaks the vertical inversion symmetry between adjacent SIO planes. This symmetry breaking facilitates significant spin-splitting of the bands, ultimately generating highly anisotropic spin textures in momentum k-space.[76]

Tuning the oxygen partial pressure during post-annealing represents another effective strategy for regulating both lattice parameters and transport properties in perovskite oxide thin films.[77,78] Following film growth, particularly for PLD, post-annealing is widely employed to optimize crystalline quality and precisely control oxygen stoichiometry. The oxygen partial pressure during annealing governs the exchange equilibrium between the film and the surrounding atmosphere,

thereby enabling controlled manipulation of oxygen-vacancy concentration. As a prevalent point defect, each oxygen vacancy nominally donates two electrons, acting as an effective electron dopant that shifts the Fermi level and modifies carrier density and type.[79] In addition to charge doping, oxygen vacancies induce local lattice distortions and charge redistribution, which can generate defect-related localized states.[80,81] Surta *et al.* reported that both the growth mode and lattice constants of SIO exhibit a pronounced dependence on oxygen partial pressure and film thickness.[82] Manca *et al.* further demonstrated that in SIO, oxygen vacancies and their associated distorted regions serve as efficient scattering centers in the parabolic bands of a notched Dirac cone, significantly reducing carrier mobility and mean free path.[83] The influence of oxygen vacancies on electronic bandwidth has also been elucidated. Suresh *et al.* showed that decreasing the oxygen partial pressure during annealing reduces the Ir–O–Ir bond angle associated with vacancy formation, leading to a narrowing of the $J_{\text{eff}} = 1/2$ bandwidth and enhanced metallic behavior within the WL regime. Moreover, electron–boson scattering in SIO films exhibits strong sensitivity to oxygen-vacancy concentration, underscoring the intricate interplay between defect-induced disorder and electron–phonon coupling.[84] Density functional theory (DFT) calculations further corroborate these observations, revealing a systematic reduction in the partial density of states at the Fermi level with increasing oxygen-vacancy concentration (Fig. 4(a)).

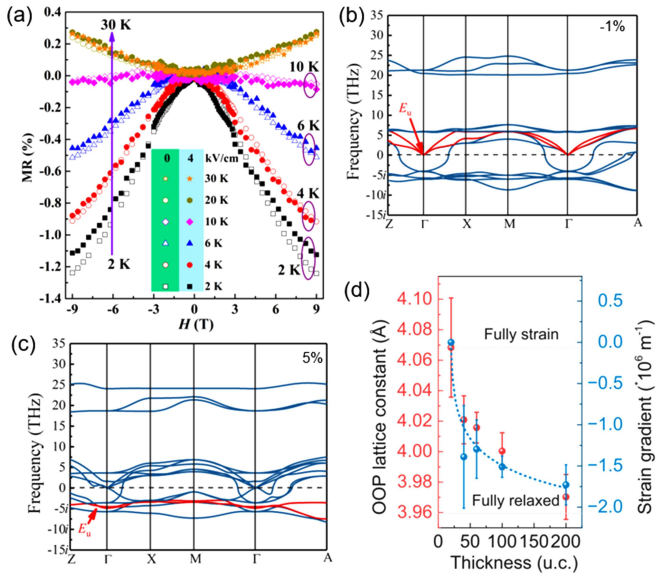


Fig. 3. (a) MR as a function of magnetic field H for 60 nm thick SIO thin films at different temperatures and gate electric fields. Reproduced with permission from Ref. [73] from AIP Publishing, Copyright 2023. (b), (c) Calculated phonon dispersion relations of tetragonal SIO under −1% and 5% strain, respectively; the presence of imaginary phonon frequencies indicates unstable phonon modes. Reproduced with permission from Ref. [75] from Elsevier, Copyright 2021. (d) Out-of-plane lattice parameter (red) and the strain-gradient value obtained from Williamson–Hall plots (blue) as a function of SIO thickness. The gray dashed lines represent the fully strained and fully relaxed limits. Reproduced with permission from Ref. [76].

Chemical doping provides an effective route to modulate carrier concentration in SIO thin films, thereby profoundly influencing charge transport, MR, and magnetic responses. In SIO, doping can shift the Fermi level, induce lattice distortions or oxygen-octahedral tilts, and reconstruct the electronic band structure, potentially leading to band-gap opening, enhanced disorder, and Anderson-type MIT. Moreover, by modifying the effective SOC strength, doping alters Berry curvature distributions, enabling regulation of anomalous Hall effects (AHEs) and MR. Beyond single-particle effects, doping also reshapes electron correlations in SIO, driving Mott-like insulating behavior, magnetic ordering, or Kondo physics. The specific magnetic nature of dopants plays a crucial role: magnetic-ion doping (e.g., Co^{2+}) tends to promote ferromagnetic (FM) correlations and enhance AHE responses, whereas AFM dopants (e.g., Cr^{3+}) may suppress long-range magnetic order, giving rise to negative MR. Overall, the transport behavior of doped SIO thin films emerges from the synergistic interplay between carrier density, lattice structure, electronic correlations, and strong SOC, greatly enriching the accessible physical phases. Precise control over dopant species and concentration enables continuous tuning from a Dirac-node semimetal to an insulating state, as well as transitions from trivial to topological electronic phases, providing a versatile platform for designing quantum materials and devices.[85] For instance, Cheng *et al.* prepared 20% Sn-doped SIO by substituting Ir^{4+} with nonmagnetic Sn^{4+} ions and observed a temperature-driven MIT accompanied by weak FM, demonstrating that Sn doping induces spin-order-related band-gap opening.[86] Subsequent studies by Cui *et al.* revealed that the AFM transition in Sn-doped SIO does not follow a conventional Mott scenario.[87,88] Instead, Sn^{4+} substitution enhances octahedral distortion, strengthens spin–spin exchange interactions, reduces SOC, and stabilizes G-type AFM ordering below the Néel temperature. The resulting weak itinerant magnetism lowers structural symmetry and opens an electronic gap at the Brillouin zone boundary, consistent with a Slater-type mechanism.[89,90] In addition to aliovalent substitution, isovalent and heterovalent B-site alloying provides further tuning flexibility. As discussed in Subsection 2.1.1, Biswas *et al.* investigated uniform $SrRuO_3$ (SRO) doping into SIO,[55] showing that modifications of the B–O–B bond angles increase the bandwidth and SOC, thereby enabling systematic control of the correlation ratio U/W. Notably, a pronounced cusp in the zero-field-cooled magnetization at approximately 25 K (Fig. 4(b)) indicates spin-glass behavior, suggesting that the perovskite $SrIr_{0.5}Ru_{0.5}O_3$ (SIRO) occupies an intermediate regime between non-Fermi-liquid and coherent Fermi-liquid states. Beyond electronic transport, doping also expands the functional landscape of SIO. Zhao *et al.* demonstrated that Co-doped SIO exhibits significantly enhanced catalytic activity for the oxygen evolution reaction,[49] attributed to unsatu-

rated IrO_x active sites generated through the dynamic dissolution of Co/Sr bimetallic ions. This result highlights the broader relevance of doping strategies in SIO for multifunctional applications spanning quantum transport, magnetism, and electrocatalysis.

Optical modulation using light fields has emerged as a powerful approach for controlling quantum materials, yielding substantial advances in the time domain, frequency domain, and detection sensitivity. Ultrafast laser excitation enables the transfer of energy, momentum, and angular momentum to condensed-matter systems, driving nonequilibrium dynamics of charge, spin, and lattice degrees of freedom. Such interactions can induce ultrafast phase transitions, photo-driven magnetization or demagnetization, and transient lattice expansion, providing unique access to light-induced quantum states beyond thermal equilibrium. Consequently, laser-field modulation has become an essential tool for probing interfacial transport phenomena in thin films and for designing optically addressable quantum devices.[72] Optical control of emergent quantum phenomena is now widely employed across quantum materials. For example, Liu *et al.* achieved a photoinduced Mott-type metal–insulator transition in perovskite SRO.[91] However, comparable studies in SIO thin films remain relatively limited. In this context, Sen *et al.* utilized laser-field modulation combined with polarization-resolved Raman scattering to investigate electron- and hole-carrier dynamics in strain-relaxed SIO films grown on $DyScO_3$ (101) substrates.[21] Their results demonstrate that the electron Raman response is well captured by marginal Fermi-liquid phenomenology (Fig. 4(c)), indicating that electron carriers — typically dominant in transport measurements — possess higher mobility than hole carriers. These findings highlight the potential of optical probes and light–matter coupling for revealing nonequilibrium transport properties and correlation effects in SIO-based heterostructures.

Ionic liquid gating (ILG) has emerged as an effective strategy for modulating transport characteristics in thin films by enabling extreme carrier doping through the formation of an electrochemical double layer.[92,93] Upon application of a gate voltage, ultrahigh charge densities can be accumulated at the film surface, leading to pronounced modifications of the electronic structure, correlation strength, and SOC.[94] Under sufficiently strong electric fields, ion migration and defect formation may also occur, driving electronic and magnetic phase transitions such as metal–insulator and paramagnetic–FM transitions.[95] At high carrier concentrations, electrostatic screening can effectively weaken SOC, thereby reshaping topological band structures and modulating transport responses, including AHE and MR. As a result, ILG provides a powerful means to simultaneously manipulate electron correlations, lattice degrees of freedom, and topological properties in SIO through the combined effects of extreme carrier doping and interfacial coupling. Gallego *et al.* demonstrated that in ultrathin SIO films, the strong electric fields generated during ILG couple intimately to the electronic structure, inducing substantial orbital reconstruction.[96] As shown in Fig. 4(d), the emergence of an AHE and the gate-induced modulation of orbital hybridization pathways, accompanied by inversion-symmetry breaking, account for the anomalous band splitting observed near the MIT. By lifting spatial inversion symmetry, the electric field opens new orbital hybridization channels, offering a distinct and efficient route for tuning correlation strength and transport behavior in SIO-based heterostructures.

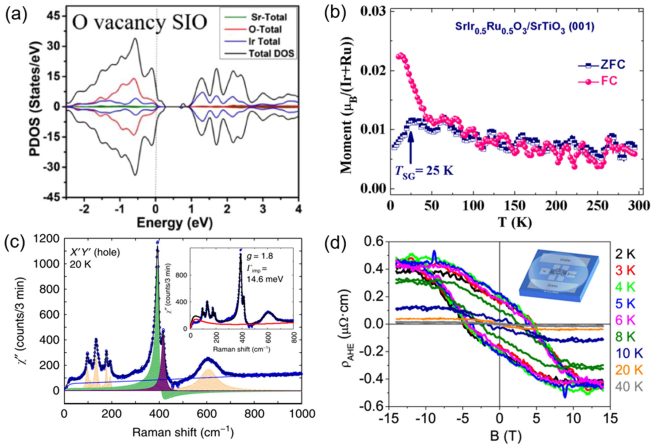


Fig. 4. (a) Computed partial density of states of a SIO thin film with oxygen vacancies on a STO substrate. Reproduced with permission from Ref. [84]. (b) Temperature dependence of the magnetic intensity of SIRO thin films grown on STO substrates measured under an applied magnetic field of 1000 Oe. Reproduced with permission from Ref. [55] from AIP Publishing, Copyright 2015. (c) Raman spectroscopy measurements of SIO films grown on $DyScO_3$ substrates, together with fits based on the Fermi-liquid mode. Reproduced with permission from Ref. [21]. (d) Anomalous Hall resistivity of SIO thin films measured from 2 K to 40 K. Reproduced with permission from Ref. [96].

2.2. Interface-driven phenomena in bilayer and multilayer heterostructures

2.2.1. Anomalous Hall effect and Rashba–Dresselhaus effect

Extensive research has focused on designing interfaces by controlling the interfacial oxide layer and harnessing interface charge transfer, thereby exploiting interface effects to modulate the magnetic and transport properties of composite oxide heterostructures. Experimental study shows that STO protectors are an effective encapsulation material that can provide stability without compromising SIO film performance.[97]

Prominent manifestations of the coupling between charge and spin degrees of freedom include the AHE, anisotropic MR, and magnetic resonance effects. Traditionally, the AHE was perceived as a signature of spontaneous magnetization in ferromagnets. However, the advent of 5d transition metal oxides has shifted this paradigm; in AFM iridates, the combination of strong SOC and broken time-reversal symmetry (often

associated with non-collinear magnetic structures) induces a substantial AHE. This phenomenon, which bridges topological physics and magnetism, is discussed in extensive detail by Yang *et al.*[98] In perovskite SIO, the influence of extrinsic mechanisms on the AHE, such as disorder-induced skew scattering and side-jump processes, is minimal. Instead, the AHE is primarily intrinsic, arising from the Berry phases associated with the electronic band structure.[99] However, in certain bilayer structures, such as SIO/$NiCo_2O_4$ heterostructures, the AHE results from the combined effects of intrinsic mechanisms dominated by Berry curvature and extrinsic mechanisms stemming from impurity scattering.[100] Jaiswal *et al.* fabricated SIO/$LaFeO_3$ heterostructures to induce robust interfacial magnetism in the SIO layer.[101] They observed characteristic AHE resistance and butterfly-shaped MR hysteresis loops, providing unambiguous evidence of emergent magnetic ordering at the interface. Using $LaCoO_3$ (LCO)/SIO bilayers and LCO/STO/SIO trilayer architectures, Jaiswal *et al.* isolated the transport properties of a single SIO layer.[102] Their findings revealed a strong, positive intrinsic AHE driven by interfacial charge transfer, as shown in Fig. 5(a), directly confirming the FM nature of the SIO interface. Yoo *et al.* utilized the $La_{0.7}Sr_{0.3}MnO_3$ (LSMO)/SIO interface to induce magnetic proximity-induced symmetry breaking (Fig. 5(b)).[103] By leveraging the strong SOC of the iridates, they synergistically generated Berry curvature hotspots at the intersections of nodal lines and energy bands. This minimal AHE model demonstrates that hole doping can further amplify topological enhancement, offering a viable strategy for the external regulation of topological states. Following the successful synthesis of (111)-oriented SIO on STO by Anderson *et al.*, Lim *et al.* further explored the system's magnetic phenomena.[104,105] They discovered that the shortened Ir–Ir bonds suppress effective SOC and bolster the density of states, thereby promoting Stoner ferromagnetism. This unique interplay allows strong SOC and ferromagnetism to emerge in tandem. The resulting compound exhibits marked magnetic anisotropy and a large Berry curvature, culminating in a distinct AHE.

The Rashba–Dresselhaus effect arises from the equivalent magnetic field generated by interface inversion asymmetry, leading to band splitting and enhancing the intrinsic spin–orbit scattering mechanism. This effect induces anisotropic transport of conducting electrons under external fields.[106] Chakraborty and Ganguli observed a strong anisotropic Rashba–Dresselhaus effect in $LaAlO_3$/SIO/STO polar/nonpolar heterostructures (Fig. 5(c)) and calculated the pseudo-spin texture using DFT+U+SOC.[107] Ganguli *et al.* systematically investigated the intrinsic correlation between the Rashba and Dresselhaus effects in this heterostructure through spin texture analysis (Fig. 5(d)), confirming that reciprocal space inversion symmetry breaking is the key source of the Rashba effect, while tilting distortion of IrO_6 octahedra introduces additional Dresselhaus-type splitting components.[108]

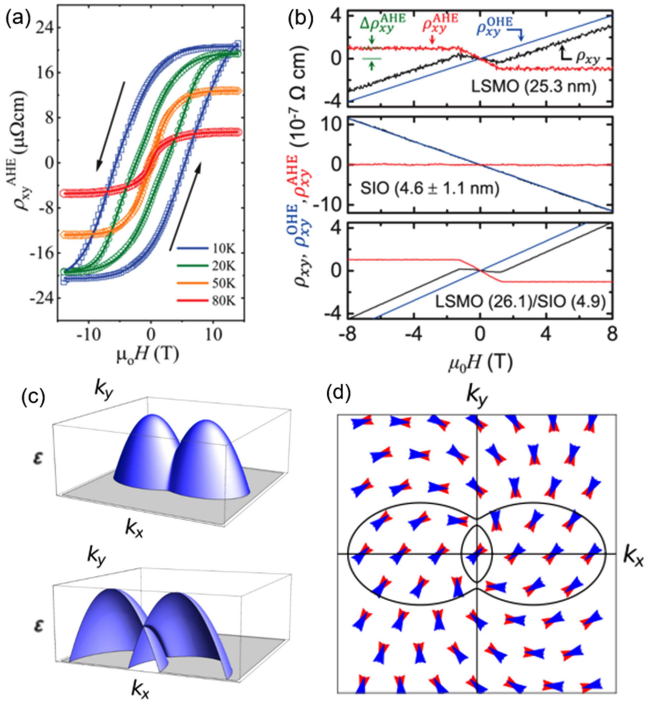


Fig. 5. (a) Magnetic-field dependence of the AHE conductivity in LCO/SIO bilayer films measured at different temperatures, together with fits using a Heaviside step-function model. Reproduced with permission from Ref. [102]. (b) Hall transport properties of LSMO and SIO monolayers, as well as the LSMO/SIO bilayer, measured at 100 K. Reproduced with permission from Ref. [103]. (c) Calculated energy–momentum dispersion of the anisotropic Rashba–Dresselhaus effect. Reproduced with permission from Ref. [107] from American Physical Society, Copyright 2020. (d) Isoenergy contours and spin textures calculated from the Rashba–Dresselhaus coupling model. Reproduced with permission from Ref. [108] from American Physical Society, Copyright 2025.

2.2.2. Spin–orbit torques and spin–charge conversion

The integration of FM layers with SIO-based SOC layers has proven to be a highly efficient architecture for generating large spin–orbit torques (SOTs). Nan *et al.* demonstrated that the spin Hall torque ratio can be precisely engineered by manipulating the octahedral tilting of the SIO lattice, enabling the design of anisotropic SHEs.[109] Building on this, Huang *et al.* realized strong effective magnetization and high SOT efficiency in LSMO/SIO heterostructures, as shown in Fig. 6(a), characterized by a significantly reduced current shunt factor.[110] The practical utility of SIO for nonvolatile memory applications is further highlighted by its performance at room temperature. Li *et al.* achieved current-induced magnetization reversal in CoFeB/SIO bilayers at low critical current densities, reporting an exceptionally high SOT efficiency ($\xi_{SOT} \approx 1.4$).[111] Furthermore, Wang *et al.* investigated SIO bilayers with Co_xTb_{1-x} alloys exhibiting perpendicular magnetic anisotropy.[112] They found that the spin-to-charge conversion efficiency (θ_{SH}) is primarily governed by the SIO/Co_xTb_{1-x} interfacial properties and remains robust

against epitaxial strain and lattice distortions induced by thickness or substrate variations.

The interface between SIO/FM bilayers often hosts complex magnetic ground states due to spin-glass-like behaviors and frustrated interactions. Yu *et al.* explored the exchange bias effect in the two-dimensional electron gas at the interface between the FM and AFM layers of SIO/LSMO bilayer films, observing a coercivity enhancement of approximately 70 times that of single-layer LSMO.[113] This dramatic increase is attributed to the formation of an interfacial spin-glass state, which arises from the strong magnetic coupling between the iridium 5d spins and the manganese 3d spins.

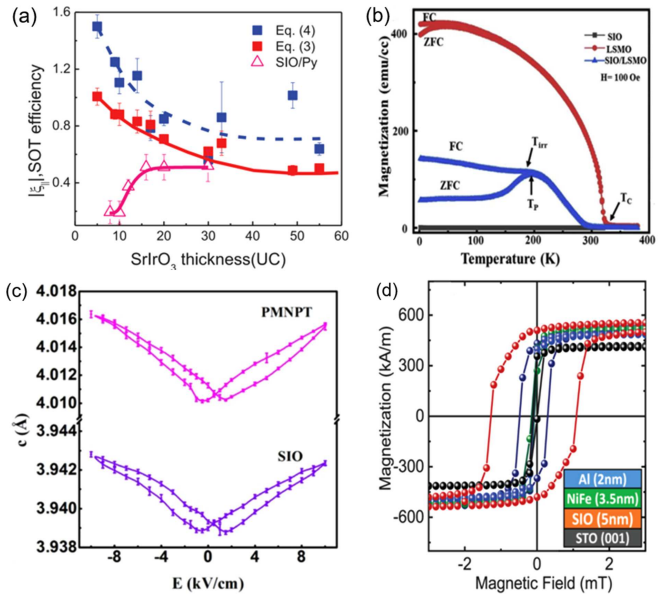


Fig. 6. (a) Dependence of the SOT efficiency on SIO thickness in LSMO/SIO heterostructures with a fixed LSMO thickness of 50 u.c. Red and blue symbols represent SOT efficiencies extracted using different analysis models, while pink symbols denote the SOT efficiency of SIO/Py bilayers. Reproduced with permission from Ref. [110] from Wiley, Copyright 2021. (b) Temperature dependence of the magnetization of SIO and LSMO monolayers, as well as the SIO/LSMO bilayer, measured under an in-plane magnetic field of 100 Oe. Reproduced with permission from Ref. [113] from Elsevier, Copyright 2019. (c) Electric-field dependence of the out-of-plane lattice parameter c of PMN–PT and SIO under an electric field applied to the PMN–PT substrate. Reproduced with permission from Ref. [115] from AIP Publishing, Copyright 2021. (d) Magnetic hysteresis loops of SIO/Py/Al multilayer films measured under an in-plane magnetic field at different temperatures. Reproduced with permission from Ref. [116] from AIP Publishing, Copyright 2020.

The high SHE in SIO has its microscopic origins in the spin Berry curvature associated with near-degenerate electronic spectra around nodal lines. This theoretical framework, analyzed by Patri *et al.* using linear response theory and tight-binding models, explains the high spin Hall conductivity observed in SIO/Py (permalloy layer, $Ni_{80}Fe_{20}$) structures.[114] Utilizing SIO as a highly efficient spin-to-charge converter, Cui *et al.* fabricated Py/SIO/PMN–PT heterostructures to detect spin currents pumped from the Py layer via the inverse spin Hall effect (ISHE).[115] By applying an external electric field to the piezoelectric PMN–PT substrate, they successfully modulated the ISHE voltage by approximately 50%. The resulting ISHE voltage exhibited a butterfly-shaped hysteresis loop, as depicted in Fig. 6(c), mirroring the strain–voltage curve of the substrate and underscoring the critical role of strain-mediated coupling in tuning spin transport.

The integrity of the FM/SIO interface is paramount for efficient spin injection. Suraj *et al.* demonstrated that the presence of an interfacial oxide layer significantly impedes the spin pumping effect in Py/SIO heterostructures.[116] Broadband FM resonance measurements revealed a sharp increase in Gilbert damping below 50 K, which was linked to enhanced spin fluctuations near the AFM ordering temperature of the interfacial oxide, as shown in Fig. 6(d). Notably, the insertion of an ultra-thin NbN buffer layer effectively suppresses this oxidation, facilitating more efficient spin current transport and damping control.

2.2.3. Topological Hall effect and chiral spin textures

The electronic band structure of SIO can be effectively reconfigured by external polarization fields. Ren *et al.* utilized the ferroelectric polarization of $PbZr_{0.2}Ti_{0.8}O_3$ (PZT) to modulate the Dirac/Weyl physics in SIO/PZT bilayers.[34] They observed an extraordinary MR effect originating from the topological band crossings, alongside a distinct negative MR at specific orientations, which is a hallmark of the chiral anomaly in Weyl semimetals (Fig. 7(a)). Similarly, the interface between nickelates and SIO provides a fertile platform for unconventional spin states. In $NdNiO_3$ (NNO)/SIO structures, Li *et al.* reported suppressed negative MR, spin-glass behavior, and a hump-like nonlinear Hall effect, suggesting the emergence of complex interfacial spin textures.[117] In $LaNiO_3$ (LNO)/SIO heterostructures, a Kondo-induced MIT was observed, as shown in Fig. 7(b), likely driven by interfacial charge transfer and the Dzyaloshinskii–Moriya interaction (DMI) fostered by the robust SOC of iridium.[118] The DMI, which arises from structural inversion symmetry breaking at interfaces, is a cornerstone of topological electronics. DMI promotes scalar spin chirality, leading to the formation of Néel-type magnetic skyrmions. These textures are typically detected via the topological Hall effect (THE), which originates from the emergent magnetic field experienced by electrons traversing a non-coplanar spin arrangement. Matsuno *et al.* investigated the THE in SRO/SIO bilayers, finding that the magnitude of the THE decreases rapidly with increasing SRO thickness.[119] This confirms that the DMI is localized at the interface. Subsequent studies by Meng *et al.* observed the zero-field THE and imaged skyrmions as small as 10 nm.[120] Using spin-polarized scanning tunneling microscopy, Corbett *et al.* directly resolved ultrasmall (3 nm) Néel skyrmions on SIO islands.[121] Their DFT calculations revealed that the SrO termination layer plays a critical role in stabilizing these columnar skyrmionic structures.

It is widely accepted that hump-like features in anomalous Hall resistance loops, reminiscent of THE signatures, indicate DMI-driven skyrmion formation. Lim *et al.* confirmed the existence of these Hall humps, showing that the peak field remains invariant as the magnetic field rotates away from the surface normal, consistent with micromagnetic simulations of Néel skyrmions.[122] While Hall humps are often attributed to skyrmions, recent studies suggest that alternative mechanisms must be considered. The sign of the DMI can be modulated by the tilting of oxygen octahedra, which plays a decisive role in the evolution of these Hall features. However, Yang *et al.* investigated SRO/SIO systems under conditions unfavorable for DMI and still observed prominent hump-like features, as illustrated in Fig. 7(c).[123] This suggests that such anomalies may not be exclusively linked to skyrmions but could instead arise from multichannel transport. In this scenario, structural inhomogeneities or variations in the local anomalous Hall coefficient across the film create independent conduction paths whose superposition mimics the THE signal. This finding underscores the need for direct imaging to definitively correlate transport anomalies with topological spin textures. In this regard, Hao *et al.* have provided a comprehensive overview of recent advances in SRO/SIO and LSMO/SIO heterostructures, synthesizing key experimental and theoretical findings within these interfacial systems.[124]

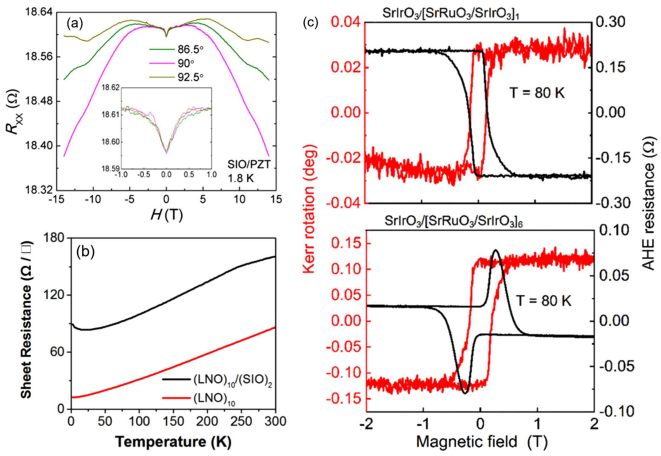


Fig. 7. (a) Negative MR and oscillations observed in SIO/PZT thin films. Reproduced with permission from Ref. [34] from AIP Publishing, Copyright 2021. (b) Temperature dependence of sheet resistance of the 10 u.c. thick LNO film and the $(LNO)_{10}/(SIO)_2$ heterostructure. Reproduced with permission from Ref. [118] from American Chemical Society, Copyright 2019. (c) AHE resistance (black) and magneto-optic Kerr effect rotation angle (red) measured at 80 K for SIO/$[SRO/SIO]_1$ and SIO/$[SRO/SIO]_6$ samples. Reproduced with permission from Ref. [123] from American Physical Society, Copyright 2021.

In addition, SIO has important applications in fast and efficient information transmission for neuromorphic computing in the field of electronic synapses. Wu *et al.* simulated various important synaptic plasticity functions through electrical stimulation of electronic synapses based on SIO epitaxial thin films by introducing PZT layers.[125] Due to the enhanced modulation of the SIO/Nb:STO interface potential barriers by polarization fields, PZT/SIO/Nb:STO devices exhibit large synaptic weights and a wide conductivity dynamic range.

2.3. Engineered quantum states in $SrIrO_3$-based superlattices

The complexity of superlattices often makes it challenging to distinguish the contributions of individual layers to the observed properties, particularly when the layers are only a few atomic layers thick. However, the favorable ground state and properties of atomically thin SIO layers provide a solid foundation for the construction of more complex structures with SOC.[126] The investigation of iridate-based superlattice structures represents a burgeoning and dynamic frontier in condensed matter physics. By achieving atomic-scale precision in chemical composition, layer thickness and stacking sequences, researchers can artificially engineer heterointerfaces and periodic architectures with unprecedented control. These systems offer a rich array of functional tuning knobs, including structural parameters, interface chemistry, epitaxial strain and external fields (electric, magnetic and optical). Such degrees of freedom enable the manifestation of novel quantum states and emergent properties that remain elusive in their bulk or single-phase counterparts.

The synthesis of complex superlattices enables the artificial manipulation of electronic structures with unit-cell precision. Nelson *et al.* systematically elucidated the electronic landscape of SIO/SRO superlattices. Their work provided a detailed mapping of interfacial charge transfer, doping profiles, and the spatial evolution of the effective carrier mass, offering a microscopic understanding of the emergent transport properties at these complex heterointerfaces.[127] Building upon the foundational work of Yang *et al.*,[123] Zheng *et al.* systematically investigated hump-shaped anomalies in the Hall resistivity of a $[(SRO)_n/(SIO)_2/(STO)_4]_5$ superlattice, as shown in Fig. 8(a).[128] Their findings reveal that the strong SOC of the Ir 5d bands near the Fermi level at the SRO/SIO interface generates a Berry curvature that counteracts the contribution from the SRO layer. As depicted in Fig. 8(b), this dual-channel model — characterized by opposing Berry curvatures — dominates the Hall response. Crucially, this mechanism provides compelling evidence that such transport features in 5d-based heterostructures can arise from topological band effects rather than exclusively from magnetic skyrmions. In summary, the observed hump-like anomalies in Hall resistivity in various SIO heterojunctions can be attributed to two primary mechanisms. The first is the intrinsic THE, which originates from the non-trivial topological magnetic structure of skyrmions. This structure generates a local Berry curvature, influencing the movement of electron carriers and producing non-zero Hall resistance signals.[122] However, this explanation cannot account for the observation of hump-type

Hall signals in SIO superlattice symmetric structures that do not exhibit skyrmions.[123] The second explanation is based on the phenomenological multi-channel anomalous Hall transport model, in which Hall signals from multiple transport channels may differ due to impurities, defects, or other non-ideal effects. Considering the interactions between these channels and the scattering processes of electrons, a hump-shaped feature can emerge in the overall Hall signal.[128] However, this model may not fully explain the hump-type Hall signal in materials that lack obvious impurities or defects. Both mechanisms offer partial explanations for the hump-type Hall signals observed in SIO heterostructures, and it is possible that they coexist.[124] Future research, including more precise experimental measurements and theoretical analyses, will be necessary to further elucidate and quantify the contributions of these two effects.

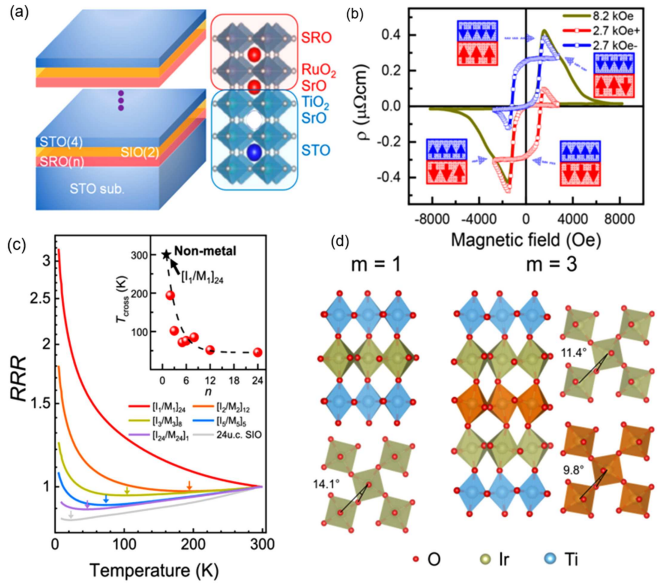


Fig. 8. (a) Crystal structure and basic physical properties of the $[(SRO)_n/(SIO)_2/(STO)_4]_5$ superlattice. Reproduced with permission from Ref. [128] from American Chemical Society, Copyright 2021. (b) AHE minor-loop measurements of $[(SRO)_6/(SIO)_2/(STO)_4]_5$ superlattices with maximum applied magnetic fields of 8.2 kOe and 2.7 kOe. Reproduced with permission from Ref. [128] from American Chemical Society, Copyright 2021. (c) Temperature dependence of the residual resistivity ratio (*RRR*), defined as $R(T)/R(300\ \mathrm{K})$, for $[I_n/M_n]_m$ superlattices, together with the functional relationship between the crossover temperature T_{cross} and the layer number n. Reproduced with permission from Ref. [129] from American Chemical Society, Copyright 2022. (d) Fully relaxed structures of $(SIO)_m$/STO superlattices. Side and top views for $m = 1$ (left) and $m = 3$ (right) illustrate thickness-dependent variations in octahedral rotations. Reproduced with permission from Ref. [130] from American Physical Society, Copyright 2021.

The competition between U and SOC represents another critical dimension in superlattice physics. Gu *et al.* explored this landscape through the metal–nonmetal crossover (MNC) in $[(SIO)_n/(CaMnO_3)_n)]_m$ superlattices.[129] As illustrated in Fig. 8(c), reducing n and modulating the superlattice periodicity simultaneously bolsters U while attenuating SOC. The resulting competition between U and SOC drives the system into the WL regime, thereby precipitating the observed MNC phenomenon. Jeong *et al.* have provided a comprehensive synthesis of recent advances in stabilizing long-range magnetic order within SIO-based heterostructures. Their review highlights the effective use of superlattice engineering to interleave SIO with various magnetic compounds, thereby inducing collective magnetic states.[126]

Furthermore, structural parameters such as the stacking sequence provide a potent means to tailor orbital anisotropy. By analyzing Ir 5d t_{2g}–O 2p orbital hybridization, Huang *et al.* demonstrated that decreasing the SIO layer number m in $(SIO)_m$/STO superlattices suppresses IrO_6 octahedral tilting while enhancing tetragonal distortion (Fig. 8(d)).[130] This evolution increases the volume fraction of the interfacial SIO layer, leading to a monotonic enhancement of orbital anisotropy. Such results underscore that the spatial extension of charge-transfer-induced metallic layers and their electronic profiles can be precisely regulated via epitaxial strain and structural design.

Hao *et al.* provided a systematic synthesis of how epitaxial strain, layer thickness, and other structural degrees of freedom dictate the interlayer coupling in SIO/STO superlattices. Furthermore, they summarized recent breakthroughs in tuning the electronic landscapes of these superlattices via ILG.[124]

In mismatched perovskite heterostructures, dislocations are not merely inevitable defects but serve as primary mechanisms for strain relaxation and functional tuning. Beyond stress relief, dislocations can accelerate ionic transport, induce bending polarization, and even trigger magnetic phase transitions, such as inducing ferromagnetism in antiferromagnets. In $[(SIO)_m/(BaTiO_3)_6]_4$ superlattices, Saghayezhian *et al.* demonstrated that the formation of edge dislocations is governed solely by the critical thickness in high-mismatch systems, independent of octahedral tilt or rotation mismatches.[131] This finding supports a novel defect engineering paradigm: utilizing localized strain from dislocations in high-mismatch layers to purposefully induce structural distortions in adjacent, low-mismatch layers.

Modifying superlattice periodicity allows for the additive design of interfacial inversion symmetry breaking, providing a direct pathway to regulate magnetic transport. Yi *et al.* observed the emergence of novel spin–orbit states and magnetization-axis reorientation in SIO by modulating its dimensionality within LSMO/SIO superlattices, thereby achieving high-precision control over magnetic anisotropy, as shown in Fig. 9(a).[132,133] Through the elaborate design of $SrTaO_3$/SIO superlattices, Zhang *et al.* demonstrated that the Ta^{4+}/Ta^{5+} mixed-valence state can induce ferromagnetism in the $SrTaO_3$ layer.[134] This ferromagnetism is further extended into the SIO layer through interfacial magnetic proximity effects. Combined with the strong SOC inherent in the 5d elements, this configuration breaks time-reversal symme-

try and yields a pronounced AHE, effectively realizing a platform where ferromagnetism and topological transport properties coexist within a single superlattice system. Similarly, in $SrMnO_3$/SIO superlattices, Nichols *et al.* identified a significant proximity-induced AHE that scales inversely with the $SrMnO_3$ layer thickness (Fig. 9(b)).[135]

The emergence of chiral magnetism and non-trivial spin textures is fundamentally tied to the DMI. Skoropata *et al.* found that periodic control of the A-site sub-lattice at the LMO/SIO interface effectively tunes the DMI strength (Fig. 9(c)), where the stability of chiral phases depends on the delicate competition between DMI, collinear ferromagnetic interactions, and magnetic anisotropy.[136] Finally, Liu *et al*. designed an SIO/LCO superlattice where the exceptionally large DMI, driven by the strong SOC of SIO, dominates over proximity-induced ferromagnetism. This manifests as the THE (Fig. 9(d)), while the itinerant ferromagnetism of SIO is simultaneously modulated via interfacial charge transfer.[137]

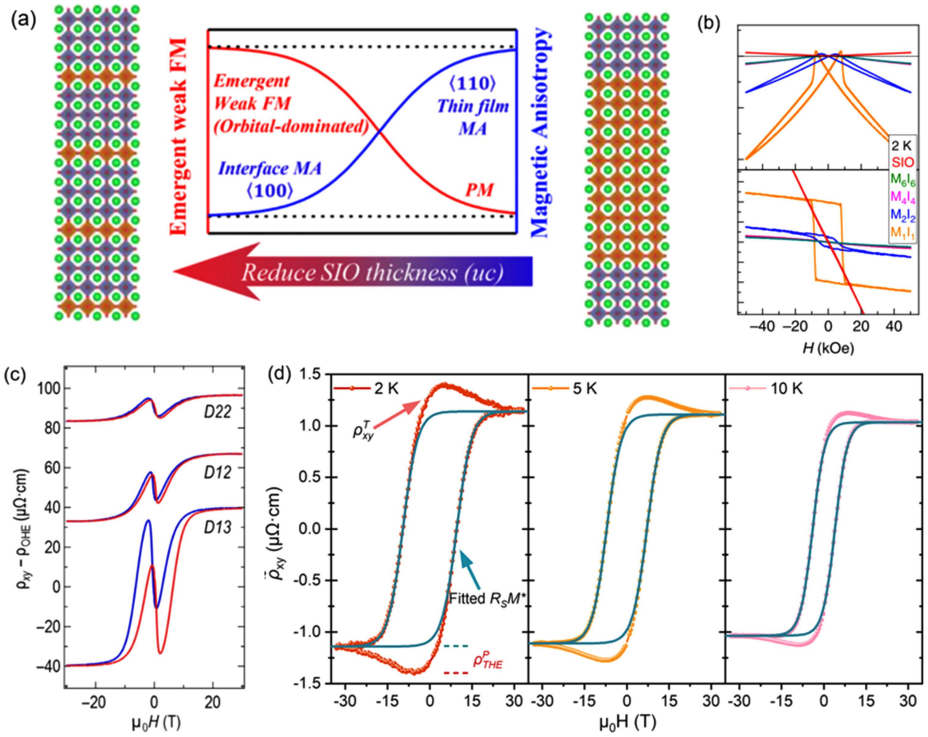


Fig. 9. (a) Thickness dependence of magnetic anisotropy in SIO superlattices. Reproduced with permission from Ref. [133]. (b) AHE measured under an in-plane magnetic field in short-period ($n \leq 6$) SMO/SIO superlattices at 2 K. Reproduced with permission from Ref. [135]. (c) Hall resistivity measured at 10 K for superlattices with different interface configurations and a fixed period of $n = 5$ u.c. Reproduced with permission from Ref. [136]. (d) AHE and THE measurements of SIO/LCO superlattices, together with the corresponding fitting results. Reproduced with permission from Ref. [137] from American Chemical Society, Copyright 2022.

3. Conclusion and perspectives

We have reviewed the current research on the transport properties of SIO. Experimental studies have revealed a rich set of physical properties in this correlated semimetal, arising from the strong interaction between SOC, moderate correlations, and structural flexibility. Theoretically, bulk SIO has been proposed as a candidate system for hosting a Weyl semimetal or topological crystalline insulator phase. The correlation-modulated $J_{\text{eff}} = 1/2$ state underpins potential topological phases, with supporting evidence provided by observations of large anomalous and nonlinear Hall effects. The synthesis of high-quality epitaxial thin films and superlattices has enabled precise control over the physical dimensionality of SIO. Research has demonstrated that strain engineering effectively influences key transport parameters, including resistivity, MR, and the MIT temperature. Furthermore, external fields such as pressure and gate voltage enable reversible tuning across the phase diagram. Recent efforts have increasingly focused on integrating SIO with other functional oxides. In such heterostructures, charge transfer, orbital reconstruction, and proximity effects can give rise to emergent properties that are absent in the individual bulk materials. Despite these advances, a direct and definitive correspondence between the observed topological transport signatures and the underlying electronic structures remains to be established through spectroscopic measurements. Theoretical models also often fall short in accurately describing the complex interplay of strong correlations, strong SOC, and electron–lattice coupling. Most investigations to date have relied on macroscopic transport measurements, which generally lack the time and spatial resolution needed to probe dynamical processes during phase transitions or under non-equilibrium conditions. Thus, it will be essential to combine advanced spectroscopic techniques with extreme-condition transport studies to directly correlate

the microscopic electronic structure with macroscopic observables. Additionally, further development of theoretical frameworks capable of simultaneously handling strong correlations, topology, and disorder is also needed. Ultimately, more work will be necessary to realize practical applications for next-generation spintronics based on SIO systems.

Acknowledgements

This research has been supported by the Fundamental Research Funds for the Central Universities (Grant No. 5000240027) and the Natural Science Basic Research Program of Shaanxi (Grant No. 2025JC-YBQN-017).

References

[1] Tokura Y and Nagaosa N 2000 *Science* **288** 462
[2] Tokura Y and Hwang H Y 2008 *Nat. Mater.* **7** 694
[3] Chow S L E, Luo Z and Ariando A 2025 *Nature* **642** 58
[4] Ohtomo A and Hwang H Y 2004 *Nature* **427** 423
[5] Chen G and Balents L 2008 *Phys. Rev. B* **78** 094403
[6] Gan Y, Yang F, Kong L, Chen X, Xu H, Zhao J, Li G, Zhao Y, Yan L, Zhong Z, Chen Y and Ding H 2023 *Adv. Mater.* **35** 2300582
[7] Zheng D, Xu J, Wang Q, Liu C, Yang T, Chen A, Li Y, Tang M, Chen M, Algaidi H, Jin C, Liu K, Kläui M, Schwingenschlögl U and Zhang X 2025 *Nano Lett.* **25** 1528
[8] Katsura H, Nagaosa N and Balatsky A V 2005 *Phys. Rev. Lett.* **95** 057205
[9] Liu X, Fang S, Fu Y, Ge W, Kareev M, Kim J W, Choi Y, Karapetrova E, Zhang Q, Gu L, Choi E S, Wen F, Wilson J H, Fabbris G, Ryan P J, Freeland J W, Haskel D, Wu W, Pixley J H and Chakhalian J 2021 *Phys. Rev. Lett.* **127** 277204
[10] Murakami S, Nagaosa N and Zhang S C 2004 *Phys. Rev. Lett.* **93** 156804
[11] Ma L, Zhou H A, Wang L, Fan X L, Fan W J, Xue D S, Xia K, Wang Z, Wu R Q, Guo G Y, Sun L, Wang X, Cheng X M and Zhou S M 2016 *Adv. Electron. Mater.* **2** 1600112
[12] Haverkort M W, Elfimov I S, Tjeng L H, Sawatzky G A and Damascelli A 2008 *Phys. Rev. Lett.* **101** 026406
[13] Chikara S, Durairaj V, Cao G, DeLong L E, Parkin S and Schlottmann P 2007 *Phys. Rev. B* **76** 100402
[14] Schofield A J 1999 *Contemp. Phys.* **40** 95
[15] Löhneysen H V, Rosch A, Vojta M and Wölfle P 2007 *Rev. Mod. Phys.* **79** 1015
[16] Biswas A, Kim K S and Jeong Y H 2016 *Perovskite Materials — Synthesis, Characterisation, Properties, and Applications* (London: Intech Open) pp. 221–259
[17] Zhang H, Haule K and Vanderbilt D 2013 *Phys. Rev. Lett.* **111** 246402
[18] Nie Y F, King P D C, Kim C H, Uchida M, Wei H I, Faeth B D, Ruf J P, Ruff J P C, Xie L, Pan X, Fennie C J, Schlom D G and Shen K M 2015 *Phys. Rev. Lett.* **114** 016401
[19] Tokura Y, Kawasaki M and Nagaosa N 2017 *Nat. Phys.* **13** 1056
[20] Dhingra A, Komesu T, Kumar S, Shimada K, Zhang L, Hong X and Dowben P A 2021 *Mater. Horiz.* **8** 2151
[21] Sen K, Fuchs D, Heid R, Kleindienst K, Wolff K, Schmalian J and Le Tacon M 2020 *Nat. Commun.* **11** 4270
[22] Stamokostas G L and Fiete G A 2018 *Phys. Rev. B* **97** 085150
[23] Liu J, Chu J H, Serrao C R, Yi D, Koralek J, Nelson C, Frontera C, Kriegner D, Horak L, Arenholz E, Orenstein J, Vishwanath A, Marti X and Ramesh R 2013 arXiv:1305.1732v1 [cond-mat.str-el]
[24] Paris E, Zhang W, Tseng Y, Efimenko A, Sahle C, Strocov V N, Skoropata E, Rolfs K, Shang T, Lyu J, Pomjakushina E, Medarde M, Rønnow H M, Normand B, Radovic M and Schmitt T 2025 *Phys. Rev. Lett.* **135** 186506
[25] Hao L, Wang Z, Yang J, Meyers D, Sanchez J, Fabbris G, Choi Y, Kim J W, Haskel D, Ryan P J, Barros K, Chu J H, Dean M P M, Batista C D and Liu J 2019 *Nat. Commun.* **10** 5301
[26] Yang J, Hao L, Meyers D, Dasa T, Xu L, Horak L, Shafer P, Arenholz E, Fabbris G, Choi Y, Haskel D, Karapetrova J, Kim J W, Ryan P J, Xu H, Batista C D, Dean M P M and Liu J 2020 *Phys. Rev. Lett.* **124** 177601
[27] Zeb M A and Kee H Y 2012 *Phys. Rev. B* **86** 085149
[28] Liu Z T, Li M Y, Li Q F, Liu J S, Li W, Yang H F, Yao Q, Fan C C, Wan X G, Wang Z and Shen D W 2016 *Sci. Rep.* **6** 30309
[29] Fujioka J, Okawa T, Yamamoto A and Tokura Y 2017 *Phys. Rev. B* **95** 121102
[30] Fang C, Chen Y, Kee H Y and Fu L 2015 *Phys. Rev. B* **92** 081201
[31] Liu J, Kriegner D, Horak L, Puggioni D, Rayan Serrao C, Chen R, Yi D, Frontera C, Holy V, Vishwanath A, Rondinelli J M, Marti X and Ramesh R 2016 *Phys. Rev. B* **93** 085118
[32] Takayama T, Yaresko A N and Takagi H 2019 *J. Phys.: Condens. Matter* **31** 074001
[33] Hsu Y T, Prishchenko D, Berben M A, Culo M, Wiedmann S R, Hunter E C, Hussey N E and Perry R S 2021 *npj Quantum Mater.* **6** 92
[34] Ren Z Y, Miao J, Zhang L P, Lv Z L, Cao J P, Jakob G, Zhou J, Chen J K, Meng K K, Li H F and Jiang Y 2021 *Appl. Phys. Lett.* **119** 112402
[35] Zhang L, Wu H, Zhou J, Wu F, Chen Y, Yao S, Zhang S and Chen Y 2013 *Appl. Surf. Sci.* **280** 282
[36] Chen Y, Lu Y M and Kee H Y 2015 *Nat. Commun.* **6** 6593
[37] Abdelaziem A, Li Z, Omar G J, Huang L, Agarwal P, Wu Y, Yan H, Beng L C, Hui H K, El-Kholy A I, Tang B, Salim T, Ariando A, Liu Z, Chia E E M and Lin K 2025 *Adv. Mater.* **37** 2417752
[38] Kim B J, Jin H, Moon S J, Kim J Y, Park B G, Leem C S, Yu J, Noh T W, Kim C, Oh S J, Park J H, Durairaj V, Cao G and Rotenberg E 2008 *Phys. Rev. Lett.* **101** 076402
[39] Liu X, Katukuri V M, Hozoi L, Yin W G, Dean M P M, Upton M H, Kim J, Casa D, Said A, Gog T, Qi T F, Cao G, Tsvelik A M, Brink J and Hill J P 2012 *Phys. Rev. Lett.* **109** 157401
[40] Rau J G, Lee E K H and Kee H Y 2016 *Annu. Rev. Condens. Matter Phys.* **7** 195
[41] Schaffer R, Lee E K H, Yang B J and Kim Y B 2016 *Rep. Prog. Phys.* **79** 094504
[42] Zhao W, Gu M, Xiao D, Li Q, Liu X, Jin K, Guo H, Meng M and Guo J 2024 *Phys. Rev. Mater.* **8** 105001
[43] Longo J M, Kafalas J A and Arnott R J 1971 *J. Solid State Chem.* **3** 174
[44] Zhang L, Pang B, Chen Y B and Chen Y 2018 *Crit. Rev. Solid State Mater. Sci.* **43** 367
[45] Biswas A, Kim K S and Jeong Y H 2014 *J. Appl. Phys.* **116** 213704
[46] Fruchter L, Schneegans O and Li Z Z 2016 *J. Appl. Phys* **120** 075307
[47] Lim Z S, Li C, Chi X, Omar G J, Ma H H, Huang Z, Zeng S, Yang P, Venkatesan T, Rusydi A, Pennycook S J and Ariando A 2020 *Nano Lett.* **20** 1890
[48] Rimal G, Tasnim T, Ortiz G C, Sterbinsky G E, Hwang J and Comes R B 2024 *Phys. Rev. Mater.* **8** L071201
[49] Zhao J W, Yue K, Zhang H, Wei S Y, Zhu J, Wang D, Chen J, Fominski V Y and Li G R 2024 *Nat. Commun.* **15** 2928
[50] Zhou L, Du Z, Wang J, Chen P, Ye B, Feng T, Yang J, Xiao Z, Yang M, Li J, Zhang W, Hai L and He H 2025 *Phys. Rev. B* **112** L241106
[51] Jaiswal A K, Eder R, Wang D, Wollersen V, Tacon M L and Fuchs D 2024 *Adv. Funct. Mater.* **34** 2308346
[52] Lu Z, Feng J, Zheng X, You S, Li R W, Autieri C, Cuoco M, Radovic M and Wang Z 2025 arXiv:2503.21093v1 [cond-mat.mes-hall]
[53] Zhang Q, Shi S, Zheng Z, Zhou H, Shao D F, Zhao T, Su H, Liu L, Shu X, Jia L, Gu Y, Xiao R, Wang G, Zhao C, Li H and Chen J 2024 *ACS Appl. Mater. Interfaces* **16** 1129
[54] Imada M, Fujimori A and Tokura Y 1998 *Rev. Mod. Phys.* **70** 1039
[55] Biswas A, Lee Y W, Kim S W and Jeong Y H 2015 *J. Appl. Phys.* **117** 115304
[56] Biswas A and Jeong Y H 2017 *Curr. Appl. Phys.* **17** 605
[57] Zhang L, Liang Q, Xiong Y, Zhang B, Gao L, Li H, Chen Y B, Zhou J, Zhang S T, Gu Z B, Yao S H, Wang Z, Lin Y and Chen Y F 2015 *Phys. Rev. B* **91** 035110
[58] Kozuka Y, Isogami S, Masuda K, Miura Y, Das S, Fujioka J, Ohkubo T and Kasai S 2021 *Phys. Rev. Lett.* **126** 236801
[59] Yun C, Li W, Gao X, Dou H, Maity T, Sun X, Wu R, Peng Y, Yang J, Wang H and MacManus-Driscoll J L 2021 *ACS Appl. Mater. Interfaces* **13** 8863
[60] Shiga D, Yang B E, Hasegawa N, Kanda T, Tokunaga R, Yoshimatsu K, Yukawa R, Kitamura M, Horiba K and Kumigashira H 2020 *Phys. Rev. B* **102** 115114
[61] Filipovic L 2019 *Microelectron. Reliab.* **97** 38

[62] McNally D E, Lu X, Pelliciari J, Beck S, Dantz M, Naamneh M, Shang T, Medarde M, Schneider C W, Strocov V N, Pomjakushina E V, Ederer C, Radovic M and Schmitt T 2019 *npj Quantum Mater.* **4** 6

[63] Stangl A 2019 *Oxygen kinetics and charge doping for high critical current YBCO films* (Ph.D. Dissertation) (Barcelona: Universitat Autònoma de Barcelona)

[64] Solovyeva V and Huth M 2011 *Synth. Met.* **161** 976

[65] Liao J, Ou Y, Feng X, Yang S, Lin C, Yang W, Wu K, He K, Ma X, Xue Q K and Li Y 2015 *Phys. Rev. Lett.* **114** 216601

[66] Liu X, Kim J W, Wang Y, Terilli M, Jia X, Kareev M, Peng S, Wen F, Wu T C, Chen H, Hu W, Upton M H, Kim J, Choi Y, Haskel D, Weng H, Ryan P J, Cao Y, Qi Y, Guo J and Chakhalian J 2024 *Nat. Commun.* **15** 10348

[67] Wu F X, Zhou J, Zhang L Y, Chen Y B, Zhang S T, Gu Z B, Yao S H and Chen Y F 2013 *J. Phys.: Condens. Matter* **25** 125604

[68] Chaurasia R, Kharkwal K C and Pramanik A K 2019 *AIP Conf. Proc.* **2142** 080008

[69] Zhang L, Chen Y B, Zhang B, Zhou J, Zhang S, Gu Z, Yao S and Chen Y 2014 *J. Phys. Soc. Jpn.* **83** 054707

[70] Groenendijk D J, Autieri C, Girovsky J, Martinez-Velarte M C, Manca N, Mattoni G, Monteiro A M R V L, Gauquelin N, Verbeeck J, Otte A F, Gabay M, Picozzi S and Caviglia A D 2017 *Phys. Rev. Lett.* **119** 256403

[71] Yang L, Wu B, Liu X, Wang M, He C, Wang S and Zhang J 2024 *Chin. Phys. Lett.* **41** 107201

[72] Sun Y T, Li M M, Wang L R, Fan Z, Guo E J and Guo H Z 2023 *Acta Phys. Sin.* **72** 096801

[73] Li S S, Zhang Y, Ying J S, Wang Z C, Yan J M, Gao G Y, Ye M and Zheng R K 2023 *J. Appl. Phys.* **133** 014104

[74] Gruenewald J H, Nichols J, Terzic J, Cao G, Brill J W and Seo S S A 2014 *J. Mater. Res.* **29** 2491

[75] Yuan Y, Fang Y W, Zhong N, Xiang P H and Duan C G 2021 *J. Magn. Magn. Mater.* **522** 167547

[76] Gu M, Sheng H, Wu X, Wu M, Liu X, Yang F, Zhang Z, Gao P, Wang Z, Meng M and Guo J 2024 *Natl. Sci. Rev.* **11** nwad296

[77] Jia C L, Thust A and Urban K 2005 *Phys. Rev. Lett.* **95** 225506

[78] Groenen R, Smit J, Orsel K, Vailionis A, Bastiaens B, Huijben M, Boller K, Rijnders G and Koster G 2015 *APL Mater.* **3** 070701

[79] Szot K, Speier W, Carius R, Zastrow U and Beyer W 2002 *Phys. Rev. Lett.* **88** 075508

[80] Kim K W, Lee J S, Noh T W, Lee S R and Char K 2005 *Phys. Rev. B* **71** 125104

[81] Chang Y J, Kim J I and Jung C U 2008 *J. Magn.* **13** 61

[82] Surta W, Almalki S, Lin Y X, Veal T and O'Sullivan M 2024 arXiv:2406.01845v1 [cond-mat.mtrl-sci]

[83] Manca N, Groenendijk D J, Pallecchi I, Autieri C, Tang L M K, Telesio F, McCollam A, Picozzi S and Caviglia A D 2018 *Phys. Rev. B* **97** 081105

[84] Suresh S, Sadhu S P P, Mishra V, Paulus W and Rao M S R 2024 *J. Phys.: Condens. Matter* **36** 425601

[85] Negishi M, Hiraoka N, Nishio-Hamane D and Takagi H 2019 *APL Mater.* **7** 121101

[86] Cheng J, Zhou J, Goodenough J B, Matsubayashi K and Uwatoko Y 2014 *JPS Conf. Proc.* **3** 013014

[87] Cui Q, Cheng J, Fan W, Taylor A, Calder S, McGuire M, Yan J, Meyers D, Li X and Cai Y 2016 *Phys. Rev. Lett.* **117** 176603

[88] Roy S B 2019 *Mott Insulators* (Bristol: IOP Publishing) pp. 1–25

[89] Mott N F 1949 *Proc. Phys. Soc. A* **62** 416

[90] Slater J C 1951 *Phys. Rev.* **82** 538

[91] Liu R, Si L, Niu W, Zhang X, Chen Z, Zhu C, Zhuang W, Chen Y, Zhou L, Zhang C, Wang P, Song F, Tang L, Xu Y, Zhong Z, Zhang R and Wang X 2023 *Adv. Mater.* **35** 2211612

[92] Song J, Chen Y, Chen X, Wang H, Khan T, Han F, Zhang J, Huang H, Zhang J, Zhang H, Zhang H, Yan X, Qi S, Hu F, Shen B, Yu R and Sun J 2019 *Phys. Rev. Appl.* **12** 054016

[93] Lin G, Wang H, Cai X, Tong W and Zhu H 2022 *ECS J. Solid State Sci. Technol.* **11** 027002

[94] Leighton C 2019 *Nat. Mater.* **18** 13

[95] Cui B, Huan Y and Hu J 2020 *J. Phys.: Condens. Matter* **32** 344001

[96] Gallego F, Tornos J, Beltran J I, Peralta A, Garcia-Barriocanal J, Yu G, Rojas G, Munuera C, Cabero M, Sanchez-Manzano D, Cuellar F, Sanchez-Santolino G, Sefrioui Z, Rivera-Calzada A, Mompean F J, Garcia-Hernandez M, Leon C, del Carmen Muñoz M and Santamaria J 2023 *Commun. Mater.* **4** 36

[97] Groenendijk D J, Manca N, Mattoni G, Kootstra L, Gariglio S, Huang Y, van Heumen E and Caviglia A D 2016 *Appl. Phys. Lett.* **109** 041906

[98] Yang J, Zhang H, Zhang H and Lin H 2023 *APL Mater.* **11** 070901

[99] Nagaosa N, Sinova J, Onoda S, MacDonald A H and Ong N P 2010 *Rev. Mod. Phys.* **82** 1539

[100] Kang P, Zhou G, Zhao Y, Ren G, Ji J, Jin C and Xu X 2025 *Sci. China Mater.* **68** 2507

[101] Jaiswal A K, Schneider R, Le Tacon M and Fuchs D 2022 *AIP Adv.* **12** 035120

[102] Jaiswal A K, Wang D, Wollersen V, Schneider R, Tacon M L and Fuchs D 2022 *Adv. Mater.* **34** 2109163

[103] Yoo M W, Tornos J, Sander A, *et al.* 2021 *Nat. Commun.* **12** 3283

[104] Anderson T J, Ryu S, Zhou H, Xie L, Podkaminer J P, Ma Y, Irwin J, Pan X Q, Rzchowski M S and Eom C B 2016 *Appl. Phys. Lett.* **108** 151604

[105] Lim J S, Autieri C, Spring M, Kamp M, Fakhredine A, Potapov P, Wolf D, Pylypenko S, Lubk A, Schultz J, Perez N, Mehlhorn B, Veyrat L, Cuoco M, Choueikan F, Ohresser P, Büchner B, Sangiovanni G, Claessen R and Sing M 2026 *Adv. Funct. Mater.* **36** e00032

[106] Sardar S, Vagadia M, Tank T M, Sahoo J and Rana D S 2024 *J. Appl. Phys.* **135** 080701

[107] Chakraborty J and Ganguli N 2020 *Phys. Rev. B* **102** 214425

[108] Ganguli N, Singh A, Kumar V and Chakraborty J 2025 *Phys. Rev. B* **111** 064413

[109] Nan T, Anderson T J, Gibbons J, Hwang K, Campbell N, Zhou H, Dong Y Q, Kim G Y, Shao D F, Paudel T R, Reynolds N, Wang X J, Sun N X, Tsymbal E Y, Choi S Y, Rzchowski M S, Kim Y B, Ralph D C and Eom C B 2019 *Proc. Natl. Acad. Sci. USA* **116** 16186

[110] Huang X, Sayed S, Mittelstaedt J, Susarla S, Karimeddiny S, Caretta L, Zhang H, Stoica V A, Gosavi T, Mahfouzi F, Sun Q, Ercius P, Kioussis N, Salahuddin S, Ralph D C and Ramesh R 2021 *Adv. Mater.* **33** 2008269

[111] Li P, Channa S, Li X, Alahmed L, Tang C, Yi D, Riddiford L, Wisser J, Balakrishnan P P, Zheng X Y, Lu D, Vailionis A, Wang S X and Suzuki Y 2023 *Phys. Rev. Appl.* **19** 024076

[112] Wang H, Meng K Y, Zhang P, Hou J T, Finley J, Han J, Yang F and Liu L 2019 *Appl. Phys. Lett.* **114** 232406

[113] Yu T, Liu Q, Chen P, Zhou L, Li H, Ning X, Qiu C and He H 2019 *J. Alloys Compd.* **789** 351

[114] Patri A S, Hwang K, Lee H W and Kim Y B 2018 *Sci. Rep.* **8** 8052

[115] Cui D, Xu Y, Zhou L, Zhang L, Luan Z, Li C, Wu D and Wu D 2021 *Appl. Phys. Lett.* **118** 052904

[116] Suraj T S, Müller M, Gelder S, Geprägs S, Opel M, Weiler M, Sethupathi K, Huebl H, Gross R, Ramachandra Rao M S and Althammer M 2020 *J. Appl. Phys.* **128** 083903

[117] Li Y, Zheng S, Liu M, Wang X, Li H, Liu J M and Wu D 2023 *J. Appl. Phys.* **134** 245301

[118] Li Y, Zhou J and Wu D 2019 *ACS Appl. Mater. Interfaces* **11** 3565

[119] Matsuno J, Ogawa N, Yasuda K, Kagawa F, Koshibae W, Nagaosa N, Yoshinori T and Kawasaki M 2016 *Sci. Adv.* **2** e1600304

[120] Meng K Y, Ahmed A, Baćani M, Mandru A O, Zhao X, Bagués N, Esser B, Flores J, McComb D, Hug H and Yang F 2019 *Nano Lett.* **19** 3169

[121] Corbett J P, Meng K Y, Repicky J J, Garcia-Diaz R, Rowland J R, Ahmed A S, Takeuchi N, Guerrero-Sanchez J, Yang F Y and Gupta J A 2022 *Appl. Surf. Sci.* **599** 153766

[122] Lim Z S, Khoo A K H, Zhou Z, Omar G J, Yang P, Laskowski R and Ariando A 2023 arXiv:2204.06174v2 [cond-mat.mtrl-sci]

[123] Yang L, Wysocki L, Schöpf J, Jin L, Kovács A, Gunkel F, Dittmann R, van Loosdrecht P H M and Lindfors-Vrejoiu I 2021 *Phys. Rev. Mater.* **5** 014403

[124] Hao L, Yi D, Wang M, Liu J and Yu P 2023 *Fundam. Res.* **3** 313

[125] Wu X, Li Z, Yi X, Jia C and Zhang W 2023 *Appl.Phys. Lett.* **123** 012104

[126] Jeong S G, Oh J Y, Hao L, Liu J and Choi W S 2023 *Adv. Funct. Mater.* **33** 2301770

[127] Nelson J N, Schreiber N J, Georgescu A B, Goodge B H, Faeth B D, Parzyck C T, Zeledon C, Kourkoutis L F, Millis A J, Georges A, Schlom D G and Shen K M 2022 *Sci. Adv.* **8** eabj0481

[128] Zheng D, Fang Y W, Zhang S, Li P, Wen Y, Fang B, He X, Li Y, Zhang C, Tong W, Mi W, Bai H, Alshareef H N, Qiu Z Q and Zhang X 2021 *ACS Nano* **15** 5086

[129] Gu M, Zhu R, Zhang X, Wang Z, An Q, Yang F, Liu X, Gao P, Meng M and Guo J 2022 *ACS Appl. Electron. Mater.* **4** 3707

[130] Huang W, Liu W, Shao Y C, Feng X, Zhang N, Fu J, Lee J M, Shen D, Chuang Y D and Liu X 2021 *Phys. Rev. B* **104** 075156

[131] Saghayezhian M, Wang Z, Howe D, Siwakoti P, Plummer E W, Zhu P Y and Zhang J 2021 *J. Phys.: Condens. Matter* **33** 275003

[132] Yi D, Tang A, Kane M M, Xu L, Liu J, Cheng Z, Klewe C, N'Diaye A T, Shafer P, Yu P, Yu R, Xu H, Lin Y, Nan C and Suzuki Y 2024 *Adv. Funct. Mater.* **34** 2313294

[133] Yi D, Liu J, Hsu S L, Zhang L, Choi Y, Kim J W, Chen Z, Clarkson J D, Serrao C R, Arenholz E, Ryan P J, Xu H, Birgeneau R J and Ramesh R 2016 *Proc. Natl. Acad. Sci. USA* **113** 6397

[134] Zhang X, Pang Z, Li Y C, Yan M, Lv Y Y, Deng Y and Zhang S T 2024 *Appl. Phys. Lett.* **124** 171904

[135] Nichols J, Gao X, Lee S, Meyer T L, Freeland J W, Lauter V, Yi D, Liu J, Haskel D, Petrie J R, Guo E J, Herklotz A, Lee D, Ward T Z, Eres G, Fitzsimmons M R and Lee H N 2016 *Nat. Commun.* **7** 12721

[136] Skoropata E, Nichols J, Ok J M, Chopdekar R V, Choi E S, Rastogi A, Sohn C, Gao X, Yoon S, Farmer T, Desautels R D, Choi Y, Haskel D, Freeland J W, Okamoto S, Brahlek M and Lee H N 2020 *Sci. Adv.* **6** eaaz3902

[137] Liu J, Zhang X, Ji Y, Gao X, Wu J, Zhang M, Li L, Liu X, Yan W, Yao T, Yin Y, Wang L, Guo H, Cheng G, Wang Z, Gao P, Wang Y, Chen K and Liao Z 2022 *J. Phys. Chem. Lett.* **13** 11946